

## Multi-wavelength study of two possible cloud-cloud collision regions: IRAS 02459+6029 and IRAS 22528+5936

Nan Li and Jun-Jie Wang

National Astronomical Observatories, Chinese Academy of Sciences, Beijing 100012, China;  
[linan@bao.ac.cn](mailto:linan@bao.ac.cn)

Received 2011 December 12; accepted 2012 March 15

**Abstract** Based on observations of  $^{12}\text{CO}$  ( $J=2-1$ ), we select targets from archived Infrared Astronomical Satellite (IRAS) data of IRAS 02459+6029 and IRAS 22528+5936 as samples of cloud-cloud collision, according to the criteria given by Vallee. Then we use the Midcourse Space Experiment (MSX) A band ( $8.28\ \mu\text{m}$ ) images and the NRAO VLA Sky Survey (NVSS) (1.4 GHz) continuum images to investigate the association between molecular clouds traced by the CO contour maps. The distribution of dust and ionized hydrogen shows an obvious association with the CO contour maps toward IRAS 02459+6029. However, in the possible collision region of IRAS 22528+5936, NVSS continuum radiation is not detected and the MSX sources are merely associated with the central star. The velocity fields of the two regions indicate the direction of the pressure and interaction. In addition, we have identified candidates of young stellar objects (YSOs) by using data from the Two Micron All Sky Survey (2MASS) in *JHK* bands expressed in a color-color diagram. The distribution of YSOs shows that the possible collision region is denser than other regions. All the evidence suggests that IRAS 02459+6029 could be an example of cloud-cloud collision, and that IRAS 22528+5936 could be two separate non-colliding clouds.

**Key words:** ISM: molecules — stars: formation — stars: individual (IRAS 02459+6029, IRAS 22528+5936) — ISM: clouds

### 1 INTRODUCTION

Stars are formed by gravitational contraction of gas in dense molecular cloud cores. How is the gravitational collapse induced? In a star forming region, the collapse could be triggered by self-gravitation or some external interaction mechanisms (Evans 1991). The first scenario of spontaneous formation suggested the clouds fragment into several clumps; when the mass of the cloud is higher than the Jeans' mass, then these dense clumps (cores), either quasi-statically or dynamically, contract to reach the mass-to-flux ratio and continue to an inside-out phase, finally forming a low-mass star (Shu et al. 1987; Mouschovias & Morton 1992). On the other hand, it has been speculated that the formation of stars is triggered by external shocks. The subgroups which belong to nearby stellar associations are spatial and temporal in order, so it suggested that star formation can also be induced by ionization-driven shocks, supernova shocks, and the stellar winds from a previous generation of OB stars (Lada et al. 1978; Blaauw 1991). Star formation triggered by cloud-cloud collisions was

also proposed as an effective external mechanism. The numerical simulation work, which depended on the parameters of the colliding cloud, found that star formation could also be induced by the cloud-cloud collisions (Hausman 1981; Gilden 1984; Lattanzio et al. 1985; Habe & Ohta 1992).

IRAS 02459+6029, which is west of the famous W5 HII region, and IRAS 22528+5936 have been mapped with  $^{12}\text{CO}(2-1)$ ,  $^{13}\text{CO}(2-1)$ ,  $^{12}\text{CO}(3-2)$ , and  $^{13}\text{CO}(3-2)$  by the Kölner Observatorium für Sub-Millimeter Astronomie (KOSMA). The W5 HII region is part of the W3/W4/W5 star formation complex in the Perseus arm. The interaction between the young, massive stars and their surroundings is studied as an interesting case of triggered star formation. In previous work, IRAS 02459+6029 has been observed with  $^{12}\text{CO}(1-0)$ ,  $^{13}\text{CO}(1-0)$  and  $\text{C}^{18}\text{O}(1-0)$ . The CO contour maps indicate that this region should be a candidate for cloud-cloud collision (Xin & Wang 2008).

## 2 OBSERVATIONS

These two sources have already been observed in  $^{12}\text{CO}(1-0)$ ,  $^{13}\text{CO}(1-0)$  and  $\text{C}^{18}\text{O}(1-0)$  with the Millimeter Telescope, which has a diameter of 13.7 m, at the Qinghai Station of the Purple Mountain Observatory, Chinese Academy of Sciences, in 2007 January. The beam size is  $50\pm 7$  arcsec in azimuth and  $54\pm 3$  arcsec in elevation. The pointing accuracy is around 5 arcsec. We used a cooled SIS mixer receiver, which has three acousto-optical spectrometers (AOSs) working at 110.20, 109.78 and 115.27 GHz to simultaneously acquire the three CO(1-0) lines. The AOS has 1024 channels, and its band widths for  $^{12}\text{CO}(1-0)$ ,  $^{13}\text{CO}(1-0)$  and  $\text{C}^{18}\text{O}(1-0)$  lines are 145.330, 42.672, and 43.097 MHz, respectively. The system temperature is 200–300 K during observations. The typical noise level of the antenna at given temperatures was 0.4 K for  $^{12}\text{CO}(1-0)$ , 0.3 K for  $^{13}\text{CO}(1-0)$  and 0.2 K for  $\text{C}^{18}\text{O}(1-0)$ . In this paper, we only use the spectra at the center (offset 0,0) of the IRAS 02459+6029 and IRAS 22528+5936 regions.

Table 1 shows the basic parameters of IRAS 22528+5936 and IRAS 02459+6029.

**Table 1** The Basic Parameters

IRAS	Galactic Coordinates		Equatorial Coordinates (J2000)		$V_{\text{LSR}}$ (km s $^{-1}$ )	$D$ (kpc)	Identification
	$l$ ( $^{\circ}$ )	$b$ ( $^{\circ}$ )	$\alpha$ (h: m: s)	$\beta$ ( $^{\circ}$ : $'$ : $''$ )			
02459+6029	136.91	1.08	02: 49: 47.6	60: 42: 07	-40	4	RAFGL 5084
22528+5936	108.79	0.25	22: 54: 49.9	59: 52: 49	-53	5.53	[PCC93] 475

The mapping data which were analyzed in this paper were observed with the KOSMA telescope in the  $^{12}\text{CO}$  ( $J=2-1$ ) (230.54 GHz) and ( $J=3-2$ ) (345.80 GHz) transitions at Gornergrat, Switzerland, in 2009 February. The dual-channel-SIS receiver with noise temperatures of 150 K and 100 K operates at 230 GHz and 345 GHz respectively. The medium and variable resolution acousto-optical spectrometers (Schieder et al. 1989) were equipped with 1501 and 1601 channels or bandwidths of 248 and 544 MHz at 230 and 345 GHz respectively. The beam size was  $130''$  and  $82''$  for 230.54 GHz and 345.80 GHz, respectively. The forward efficiency  $F_{\text{eff}}$  was about 90% during our observations. The beam efficiency was 0.68 and 0.70 for the two frequencies. For an efficient mapping, the two source observations use the on-the-fly (OTF) observing mode. The two regions were mapped on a grid with a spacing of  $60''$  for each step, and the integration time was 8 seconds. The map's central position is (RA (2000)= $02^{\text{h}}49^{\text{m}}47.6^{\text{s}}$ , Dec (2000)= $60^{\circ}42' 07.26''$ ) for IRAS 02459+6029, and (RA (2000)= $22^{\text{h}}54^{\text{m}}49.9^{\text{s}}$ , Dec (2000)= $59^{\circ}52' 49''$ ) for IRAS 22528+5936. The data reduction uses the software packages CLASS (Continuum and Line Analysis Single-disk Software) and GREG (Grenoble Graphic).

### 3 DATA REDUCTION

#### 3.1 The Molecular Line Spectra and Selection of Sources

The two sources were identified by the spectral lines of CO and its isotopes.

Figure 1 shows the  $^{12}\text{CO}$ ,  $^{13}\text{CO}$  and  $\text{C}^{18}\text{O}$  ( $J=1-0$ ) spectra at the center of the IRAS 02459+6029 and IRAS 22528+5936 regions. Both the figures show that the different optically thick lines of each source have similar profiles. The  $^{12}\text{CO}$ ,  $^{13}\text{CO}$  and  $\text{C}^{18}\text{O}$  ( $J=1-0$ ) spectra have double-peaked main lines and the peaks are located at almost the same velocity. Several factors could induce the double-peaked line profile in optically thick  $^{12}\text{CO}$  lines, which includes self-absorption, outflow, infall, rotation, a two cloud configuration, etc. People have already compared and contrasted the spectral profile of  $^{12}\text{CO}$  with the profiles of  $^{13}\text{CO}$  and  $\text{C}^{18}\text{O}$ , and they have summarized their differing features (Zhou et al. 1993; Dobashi et al. 1993; Walsh et al. 2002; Xin & Wang 2008). Toward the two sources, the profile of the optically thick  $^{12}\text{CO}$  lines fit the profiles of the optically thin  $^{13}\text{CO}$  and  $\text{C}^{18}\text{O}$  cases very well. So the possibility of self-absorption, outflow, infall and rotation is remote. It could be two separated clouds in a double-peaked profile region.

#### 3.2 The $^{12}\text{CO}$ ( $J=2-1$ ) Spectra, Integrated Intensity Map and the Position-velocity Diagrams

Figure 2 presents the  $^{12}\text{CO}$  ( $J=2-1$ ) line spectra of the two sources. Because the  $^{13}\text{CO}$  ( $2-1$ ) spectra of IRAS 22528+5936 are missing due to bad weather, and the  $^{12}\text{CO}$  ( $3-2$ ) spectra of IRAS 02459+6029 have bad signal-to-noise ratios, we only have to the  $^{12}\text{CO}$  ( $2-1$ ) spectra and contour map available for analysis. We want to know more details about the clouds' interaction regions, such as possible kinematics, star formation activities, and so on. First, we concentrate on the contour maps and the position-velocity diagrams of the two sources. The integrated intensity maps of IRAS 02459+6029 and IRAS 22528+5936 (Fig. 3), and the position-velocity diagrams of the two sources (Fig. 4) are all judged by the criteria given by Vallee (1995a). According to the criteria, the two velocity components of each source are adjacent to each other in space and velocity respectively. This means the two sources could be considered as candidates for regions showing cloud collision, although the position-velocity (P-V) diagram of IRAS 22528+5936 does not reveal the adjacency in velocity very well.

#### 3.3 Derived Parameters

Observed parameters of the two sources have been listed in Tables 1 and 2 respectively.  $T_{\text{R}}^*(12)$  and  $T_{\text{R}}^*(13)$  are the  $^{12}\text{CO}$  and  $^{13}\text{CO}$  ( $1-0$ ) radiation temperature:  $T_{\text{R}}^* = T_{\text{A}}^*/\eta_{\text{mb}}$ , where  $T_{\text{A}}^*$  is the antenna temperature corrected with atmospheric attenuation and other losses (these are performed by the observatory), and  $\eta_{\text{mb}}$  is the main beam efficiency.  $v_{13}$  is the Gaussian fit of  $V_{\text{LSR}}$  ( $^{13}\text{CO}$ ) and  $\Delta v_{13}$  is its full width at half maximum (FWHM). The cores' distances from us are obtained from the literature (Wouterloot & Brand 1989). The size  $d$  is the angular diameter of a circle whose area is equal to that of the cloud core. The  $^{12}\text{CO}$  ( $1-0$ ) line is usually considered as being optically thick in massive CO cores. Assuming local thermodynamic equilibrium (LTE), the excitation temperature  $T_{\text{ex}}$  of the  $^{13}\text{CO}$  ( $1-0$ ) transition is the same as that of the  $^{12}\text{CO}$  one (Garden et al. 1991).

$$T_{\text{ex}} = \frac{h\nu}{k} \left\{ \ln \left[ 1 + \left( \frac{kT_{\text{R}}^*(^{12}\text{CO})}{h\nu} + \frac{1}{\exp(\frac{h\nu}{kT_{\text{bg}}} - 1)} \right)^{-1} \right] \right\}^{-1}, \quad (1)$$

where  $T_{\text{bg}}=2.7$  K. The  $^{13}\text{CO}$  ( $1-0$ ) transition is usually optically thin. On the assumption of LTE, the opacity of  $^{13}\text{CO}$  ( $1-0$ ) is approximately

$$\tau(^{13}\text{CO}) \approx -\ln \left[ 1 - \frac{T_{\text{R}}^*(^{13}\text{CO})}{T_{\text{R}}^*(^{12}\text{CO})} \right]. \quad (2)$$

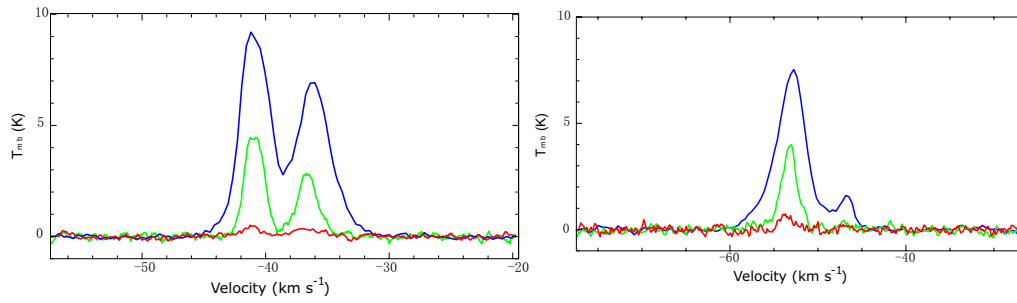


**Fig. 1** *Left:* the  $^{12}\text{CO}$  (blue),  $^{13}\text{CO}$  (green) and  $\text{C}^{18}\text{O}$  ( $J=1-0$ ) (red) spectra of IRAS 02459+6029 show the double-peaked main lines at  $-41$  and  $-36$   $\text{km s}^{-1}$ . *Right:* the spectra of IRAS 22528+5936 also have double-peaked main lines at  $-53$  and  $-47$   $\text{km s}^{-1}$ .

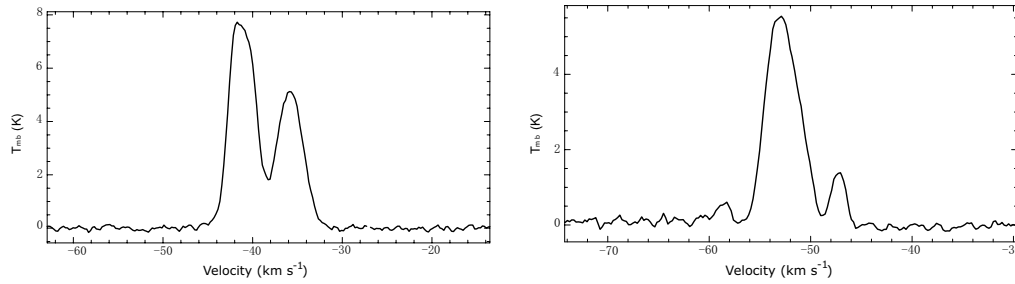


**Fig. 2** *Left:* the spectra show the double-peaked main lines at  $41.7$   $\text{km s}^{-1}$  and  $35.5$   $\text{km s}^{-1}$  with  $^{12}\text{CO}(J=2-1)$  at the center of the IRAS 02459+6029 region. *Right:* for the  $^{12}\text{CO}(J=2-1)$  double-peaked spectra of IRAS 22528+5936, the peaks lie at  $53$   $\text{km s}^{-1}$  and  $47$   $\text{km s}^{-1}$  respectively.

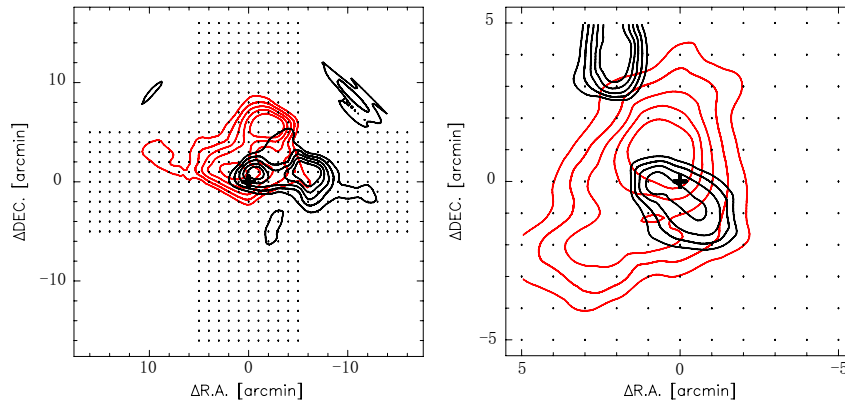


**Fig. 3** *Left:* the  $^{12}\text{CO}$  ( $J = 2 - 1$ ) contour map for IRAS 02459+6029. The red solid contours indicate the integrated intensities over the velocity from  $-47.2$   $\text{km s}^{-1}$  to  $-38.1$   $\text{km s}^{-1}$ . The black solid contours mark the velocity from  $-38.1$   $\text{km s}^{-1}$  to  $-30.2$   $\text{km s}^{-1}$ . *Right:* the contour map toward IRAS 22528+5936. The two velocity components are marked with red and black solid contours respectively. The red one shows the integrated intensity scale covering the velocity from  $-61.7$   $\text{km s}^{-1}$  to  $-48.8$   $\text{km s}^{-1}$ , and the black contours show the integrated range from  $-48.8$   $\text{km s}^{-1}$  to  $-44.8$   $\text{km s}^{-1}$ . Both of them set the contour levels at 30%, 40%, 50%.....90% of the peak intensity. The plus symbols show the positions of the IRAS sources, and the small dots show the mapped area.

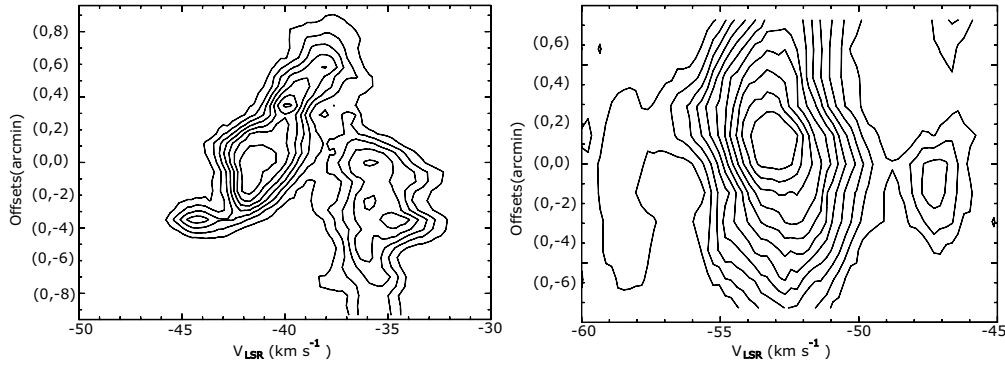


**Fig. 4** *Left*: the position-velocity diagram of IRAS 02459+6029 is constructed with CO( $J = 2 - 1$ ). The contour levels increase from 1K to 8K by steps of 1K. *Right*: the P-V diagram of IRAS 22528+5936. The contour levels are presented from 0.5K to 5.5K with steps of 0.5K.

Sometimes the  $^{12}\text{CO}$  spectra are self-reversed by absorption from the cold part of the outer cloud core. In that case the  $^{13}\text{CO}$  opacity will be underestimated. The  $^{13}\text{CO}$  column density is given by

$$N(^{13}\text{CO}) = \frac{3k}{8\pi^3 B\mu^2} \frac{\exp[\frac{hBJ(J+1)}{kT_{\text{ex}}}]}{J+1} \times \frac{T_{\text{ex}} + hB/3k}{[1 - \exp(\frac{-h\nu}{kT_{\text{ex}}})]} \int \tau_{\nu} d\nu, \quad (3)$$

where  $B$  is the rotational constant of  $^{13}\text{CO}$ ,  $\mu$  is the permanent dipole moment and  $J$  is the rotational quantum number of the lower state (Garden et al. 1991). We adopt the  $^{12}\text{CO}$  and  $^{13}\text{CO}$  abundances to be

$$\frac{N(\text{H}_2)}{N(^{12}\text{CO})} = 10\,000, \quad \frac{N(^{12}\text{CO})}{N(^{13}\text{CO})} = 89. \quad (4)$$

The mass of a  $^{13}\text{CO}$  core is proportional to its area and peak column density. Supposing that the core is spherical and the volume density is uniform, the estimated core mass is then

$$M_{\text{LTE}} = \frac{2\pi}{3} R^2 \mu_g m_{\text{H}_2} N(\text{H}_2), \quad (5)$$

where  $\mu_g = 1.36$  is the mean atomic weight and  $m_{\text{H}_2}$  is the mass of a hydrogen molecule. Assuming that the cloud core is a gravitationally bound isothermal sphere with uniform density and is supported solely by random motion, there is a relation between core mass and velocity dispersion given by the virial theorem (Ungerechts et al. 2000)

$$\frac{M_{\text{vir}}}{M_{\odot}} = 2.10 \times 10^2 \left(\frac{R}{\text{pc}}\right) \left(\frac{\Delta v}{\text{km s}^{-1}}\right)^2. \quad (6)$$

The infrared luminosity can be calculated by (Elitzur et al. 1989)

$$L_{\text{ir}} = (20.653 \times F_{12} + 7.358 \times F_{25} + 4.578 \times F_{60} + 1.762 \times F_{100}) \times D^2 \times 0.30, \quad (7)$$

where  $D$  is the distance from the Sun in kpc, and  $F_{12}, F_{25}, F_{60}, F_{100}$  are the infrared fluxes at the four IRAS bands (12 $\mu\text{m}$ , 25 $\mu\text{m}$ , 60 $\mu\text{m}$ , 100 $\mu\text{m}$ ) which are given in the IRAS point source catalog, respectively.

Derived parameters of the two sources are listed in Table 3.  $T_{\text{ex}}$  is the excitation temperature calculated from  $^{12}\text{CO}(1-0)$ .  $N_{\text{H}_2}$  is the column density,  $\tau_{13}$  is the  $^{13}\text{CO}(1-0)$  opacity,  $R$  is the core size,  $M$  is the core mass,  $M_{\text{vir}}$  is the virial mass and  $L_{\text{ir}}$  is the infrared luminosity.

**Table 2** The Basic Parameters of the Cores in the Two Sources

IRAS	RA(2000) (h: m: s)	Dec.(2000) (°: ': ")	$T_{\text{R}}^*(^{12}\text{CO})$ (K)	$T_{\text{R}}^*(^{13}\text{CO})$ (K)	$v_{13}$ (km s <sup>-1</sup> )	$\Delta v_{13}$ (km s <sup>-1</sup> )	$D$ (kpc)	$d$ (arcmin)
02459+6029 A	02: 49: 47.6	60: 42: 07	18.45	9.23	-40.92	1.9	4	2.1/ 2
02459+6029 B			13.21	5.34	-36.57	1.9		1/ 1.5
22528+5936 A	22: 54: 49.9	59: 52: 49	14.78	7.75	-53.25	2.1	5.53	3.5
22528+5936 B			3.26	1.02	-46.98	1.3		1.8

**Table 3** The Derived Parameters of These Cores

Core Name	$T_{\text{ex}}$ (K)	$N_{\text{H}_2}$ (10 <sup>22</sup> cm <sup>-2</sup> )	$\tau_{13}$	$R$ (pc)	$M$ (10 <sup>4</sup> $M_{\odot}$ )	$M_{\text{vir}}$ (10 <sup>3</sup> $M_{\odot}$ )	$L_{\text{ir}}$ (10 <sup>3</sup> $L_{\odot}$ )
02459+6029 A-1	26.40	4.40	0.69	2.41	1.16	1.83	11.54
02459+6029 A-2				2.33	1.08	1.77	
02459+6029 B-1	21.13	2.18	0.52	1.16	0.13	0.88	5.90
02459+6029 B-2				1.75	0.30	1.33	
22528+5936 A	22.71	3.92	0.74	4.02	2.87	3.72	5.90
22528+5936 B	11.07	0.33	0.38	2.09	0.07	0.74	

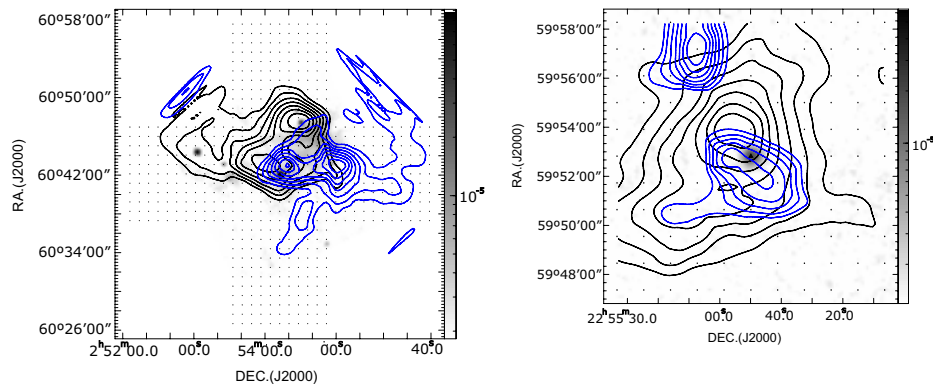
### 3.4 Multi-Wavelength Data Analysis

In order to investigate the correlation between possible star formation activities and cloud-collision phenomena, the multi-wavelength results will be of assistance to future studies. Thus, we combine the data from the Midcourse Space Experiment (MSX) images, the NRAO VLA Sky Survey (NVSS), the Infrared Astronomical Satellite (IRAS) and the Two Micron All Sky Survey (2MASS). By overlaying the contour map, the MSX A-band image shows us information about the dust and the association with the cloud-collision region (Fig. 5). The NVSS 1.4 GHz continuum survey images are also overlaid on the CO( $J=2-1$ ) contour maps for the two sources (Fig. 6). In addition to the image, we have analyzed the velocity of the mapping points for IRAS 02459+6029 and IRAS 22528+5936, then plot the velocity fields of the two regions (Fig. 7). In Figure 7 (left), the velocity contours indicate a maximum in the gradient of the velocity field in the vicinity of the interaction region, where the two components overlap each other. The trends in density for the contour lines show the direction of interactions in the two colliding clouds. In order to clearly reveal the intensity scale for the two components of IRAS 22528+5936, Figure 7 (right) uses a map with colored scales instead of contour lines for one component.

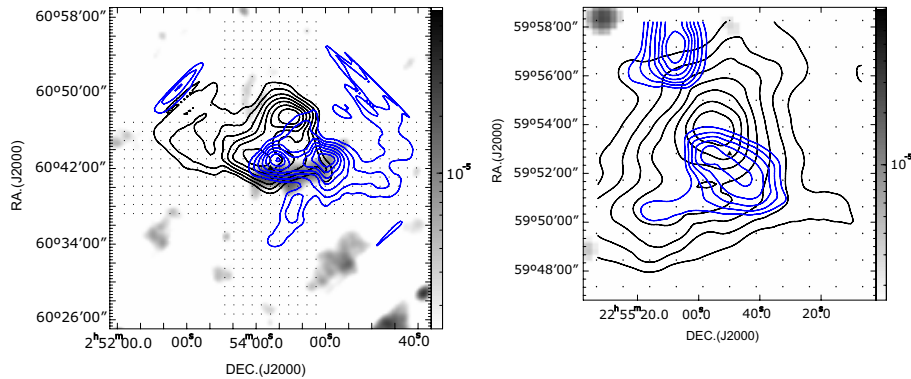
For further investigation of star formation in the two regions, we focus on the distribution of young stellar objects (YSOs) in these two regions. The 2MASS color-color diagram in  $JHK$  bands is a good tool to select the YSOs.

Figure 8 is the color-color plot for the two regions. The classical T Tauri stars (CTTSs) (Herbig & Bell 1988) are found to lie approximately between the two parallel dotted lines, which are defined empirically by  $(j_m - h_m) - 1.7(h_m - k_m) + 0.0976 = 0$  and  $(j_m - h_m) - 1.7(h_m - k_m) + 0.450 = 0$ , where  $j_m$ ,  $h_m$  and  $k_m$  are 2MASS magnitudes, and the slope is specified by the interstellar reddening law (Rieke & Lebofsky 1985). The dash-dotted line shows the dereddened CTTS locus (Meyer et al. 1997), modified for use in 2MASS photometry (Carpenter 2001), with  $(j_m - h_m) - 0.493(h_m - k_m) - 0.439 = 0$ . After using the color-color diagram to pick the candidate YSOs, we construct a contour map showing the density distribution of YSOs (Fig. 9).

Figure 9 (left) is the gray-scale map of the distribution density superimposed onto the CO( $J=2-1$ ) intensity contour map. It clearly shows the clumps with increasing density which are associated with the interacting region of the two components in the vicinity of IRAS 02459+6029. Comparatively speaking, the right map is the map of density distributions overlaid on the contours of CO intensity for IRAS 22528+5936. The density clumps are located at the center, in almost the



**Fig. 5** The integrated intensity maps are overlaid on the MSX 8.28(A band) images (gray-scale map) toward IRAS 02459+6029 (*left*) and IRAS 22528+5936 (*right*). The triangle marks the center of the mapped region.



**Fig. 6** The figures show the contour maps of the two sources, IRAS 02459+6029 (*left*) and IRAS 22528+5936 (*right*), superposed on the NVSS 1.4 GHz continuum survey images, which are represented by gray-scale maps. The center of the mapped region is labeled with a triangle.

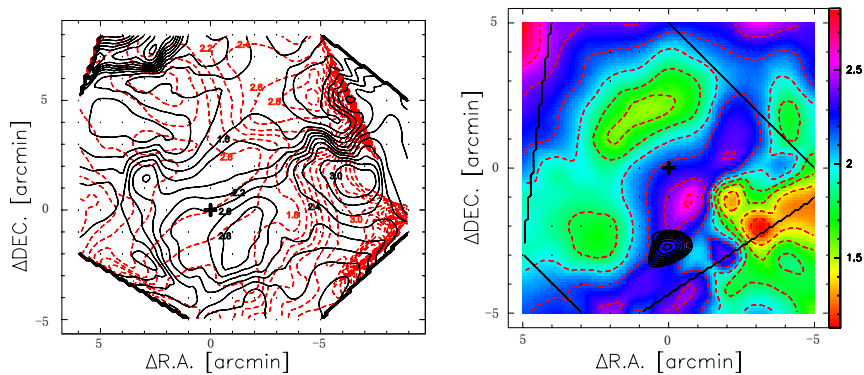


**Fig. 7** *Left* contour map showing the  $^{12}\text{CO}(J=2-1)$  velocity field of IRAS 02459+6029. The red dotted line shows one velocity component, and the black solid line represents the other component. The velocity field of IRAS 22528+5936 (*right*) is also described by two components. In the color-scale map, the red dotted line and the black solid line represent two different components. Both central positions of the two sources are plotted by plus signs. The contour levels are given from 0 to 3 with a step of 0.2 (the value is the relative change).

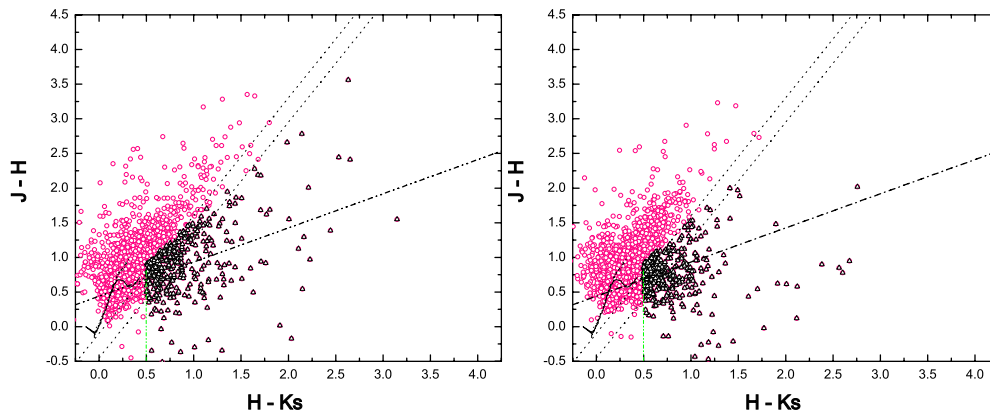


**Fig. 8** The two figures are 2MASS color-color diagrams in  $JHK$  bands used for selection of YSOs. The left one is for the IRAS 02459+6029 region, and the right one is for the IRAS 22528+5936 region. The solid line traces the path of the main-sequence (Lada 1992). The two dotted parallel lines have slopes derived from the interstellar reddening law (Rieke & Lebofsky 1985). Three lines separate CTTSs from Herbig Ae/Be and reddened main-sequence stars. The dash-dotted line is the locus of dereddened CTTS (Lee et al. 2005). The green dotted line is derived from the empirical value. The pink circles show all the 2MASS point sources in these regions. The selected ones are colored black with an open triangle shape.

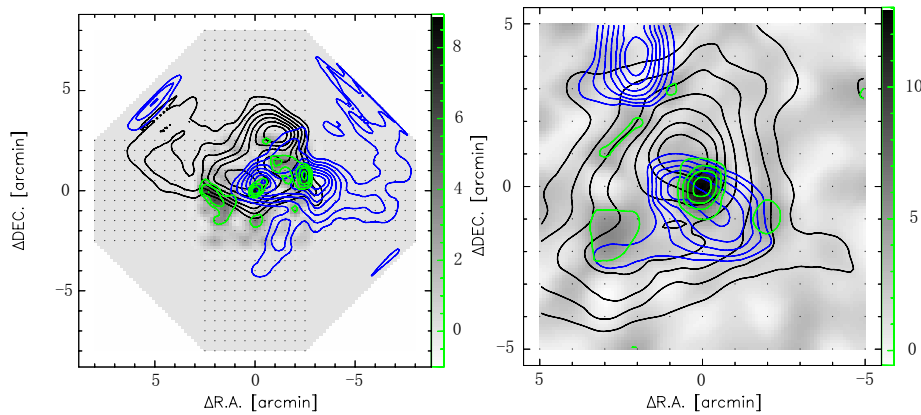


**Fig. 9** The gray-scale maps combined with green contours in the vicinity of IRAS 02459+6029 (*left*) and IRAS 22528+5936 (*right*) show the density of the selected YSOs in these regions. The black and blue contour lines indicate the CO( $J=2-1$ ) ranges of integrated intensity.

same position as IRAS 22528+5936. The shape of the clump is not similar to the shape of the collision region. Why does the density clump have this kind of shape? We need more information about YSOs to answer such a question. We perform the color cuts used for the IRAS sources in our two regions under investigation. The color cuts used here were derived from values in the literature and were taken from studies of several types of objects: T Tauri stars, low-mass and intermediate-mass YSOs, as well as massive YSOs.

Table 4 lists the color cuts we used. We use the criteria to select the YSO candidates, but it is not a unique classification method. The choice of color cuts is merely meant to be as inclusive as possible. All the results are listed in Tables 5 and 6 and represented in Figure 10.

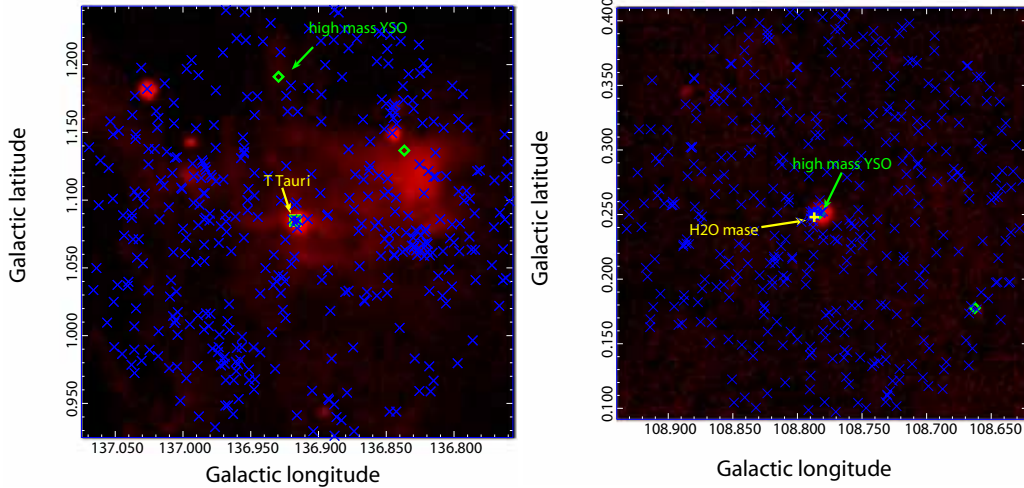


**Fig. 10** The two figures show us the MSX images in the vicinities of IRAS 02459+6029 (*left*) and IRAS 22528+5936 (*right*). The high mass star is marked with a green diamond. The T Tauri star is plotted by a yellow box, and the H<sub>2</sub>O maser is represented by a yellow plus. The blue cross symbols show us the candidates of YSOs from 2MASS data.

**Table 4** IRAS Color Cuts Used for the Selection Of YSOs

Object Type	[25–12]	[60–25]	[100–60]	Reference
T Tauri stars	0–0.6	<0.5	...	[1, 2]
Intermediate-mass YSOs	0–1.0	0.4–1.0	...	[3]
High-mass YSOs	0.17–1.5	0.23–1.13	0.08–0.57	[4]

Where  $[\lambda_1 - \lambda_2] = \log(F_{\lambda_1}/F_{\lambda_2})$ . [1] Harris et al. (1988). [2] Prusti et al. (1992). [3] Beichman et al. (1986). [4] Bronfman et al. (1996).

**Table 5** The Classification of YSOs in IRAS 02459+6029

YSO Coordinates (J2000)		[25–12]	[60–25]	[100–60]	Type
RA	Dec.				
42.5666	60.7918	0.38	0.99	0.49	High Mass
42.3468	60.7837	0.67	0.84	0.30	High Mass
42.4484	60.7019	0.41	0.44	0.28	T Tauri

**Table 6** The Classification of YSOs in IRAS 22528+5936

YSO Coordinates (J2000)		[25–12]	[60–25]	[100–60]	Type
RA	Dec.				
343.5559	59.7619	0.12	0.99	0.61	Intermediate Mass
343.7077	59.8801	0.60	0.69	0.18	High Mass

In Figure 10, the two plots show the MSX images with the 2MASS YSO candidates and the IRAS sources for IRAS 02459+6029 and IRAS 22528+5936. For IRAS 02459+6029, the very massive stars are not located in the overlapping region, and the interaction area in the two components is associated with the diffuse MSX feature. However, for IRAS 22528+5936, the map's center is a high-mass star, and the MSX clumps are clearly superposed on it. It is also the region with interactions in the two components.

#### 4 DISCUSSION

In this paper, we select two IRAS sources to investigate the regions with cloud-cloud collisions. The two regions are mapped around IRAS 02459+6029 and IRAS 22528+5936. In the SIMBAD database, IRAS 22528+5936 is identified as a galaxy. According to our check, there were 16 citations to this object between 1980 and 2012. IRAS 22528+5936 is located in the Cepheus clouds. Most references treat IRAS 22528+5936 as a point source, and IRAS 22528+5936 is selected from 1331 cold IRAS sources (Yang et al. 2002). We calculate the infrared luminosity of IRAS 22528+5936; it is less than the minimum infrared luminosity of the galaxy (by about  $10^6 L_{\odot}$ ), so we treat IRAS 22528+5936 as a cloud which contains YSOs.

We compare and contrast the two regions by using different analysis methods. First, we consider that the two regions are good samples for the cloud-cloud collision study according to the criteria given by Vallee (1995a) because their CO( $J=2-1$ ) contour map and P-V diagram are adjacent in space and velocity, respectively. Then, the MSX images (8.28 $\mu$ m) are overlaid on the CO contour maps. The MSX band A is used for a higher resolution dust (and polycyclic hydrocarbon [PAH]) image. For IRAS 02459+6029, we see that the diffuse MSX dust is clearly associated with the collision region. In another source region, the MSX image is just located at the central position of IRAS 22528+5936. The NVSS 1.4 GHz data reveal information about ionized hydrogen. Thus in Figure 6 (left), we notice that the trunk figure lies in the overlapping region of the two components. However, for the right map, in the CO contour region, there is no 1.4 GHz continuum image. The 2MASS point catalog has been used to identify sources which have colors indicating the presence of YSOs. The 2MASS color-color diagrams in  $JHK$  bands are used to select the YSO candidates in these two regions. Based on this, we calculate the density of the YSOs. Figure 9 (left) shows us the density increases in the interacting region for IRAS 02459+6029. The right one reveals a sudden increase at the center of the map upon which IRAS 22528+5936 is located. In addition, the color cuts are used to classify the IRAS point catalog which our region covers.

All the evidence suggests that: 1. IRAS 02459+6029 could be a cloud-cloud collision region and there is a potential star forming region. Many YSOs are detected in the colliding region which could be triggered by cloud collision. 2. Then we focus on the IRAS 22528+5936 region. Although the two clouds are adjacent in space and velocity, the MSX image shows a globular dust clump encircling the central star, and NVSS data do not appear in this area. According to the colors of YSOs in the IRAS catalog, the central star is a massive star which is associated with an H<sub>2</sub>O maser. If the star is a massive star with no ionized hydrogen around it, maybe the molecular clouds have already been blown away. Thus we consider that the IRAS 22528+5936 region reveals two interacting components which are coincident in the line of sight. There is possibly some distance between the two clouds.

#### 5 CONCLUSIONS

In this paper, we use several methods including the criteria given by Vallee (1995b) to detect candidates for cloud collision. Some of the methods are developed by ourselves and used in the study of cloud collision for the first time. These new criteria are helpful and significant for investigating cloud-cloud collisions because it is difficult to measure the distance between the two clouds. In order to find out if these two clouds are colliding or just overlapping in the line of sight, we can use the criteria given by

- (1) We could describe the velocity field in the interacting region, to see if there are velocity gradients showing the direction of the pressure and interaction between the clouds.
- (2) We could use the density map of YSOs in this region, to see if the number of YSOs is suddenly increasing somewhere. Further, we could check if this dense area is similar to the colliding area in terms of morphology.

- (3) We could investigate the superposed map of multi-wavelength data to see if there is an obvious association between them.

As a consequence of the above, IRAS 02459+6029 is suggested to be a cloud-cloud collision region where many YSOs could be triggered by collision, but IRAS 22528+5936 cannot be such a case. In future work, we will develop more methods to distinguish and confirm the collision region, and try to better understand all the associated astrophysical processes.

## References

- Beichman, C. A., Myers, P. C., Emerson, J. P., et al. 1986, *ApJ*, 307, 337
- Blaauw, A. 1991, in *NATO ASIC Proc. 342: The Physics of Star Formation and Early Stellar Evolution*, eds. C. J. Lada & N. D. Kylafis, 125
- Bronfman, L., Nyman, L.-A., & May, J. 1996, *A&AS*, 115, 81
- Carpenter, J. M. 2001, *AJ*, 121, 2851
- Dobashi, K., Onishi, T., Iwata, T., et al. 1993, *AJ*, 105, 1487
- Elitzur, M., Hollenbach, D. J., & McKee, C. F. 1989, *ApJ*, 346, 983
- Evans, N. J., II 1991, in *Frontiers of Stellar Evolution*, *Astronomical Society of the Pacific Conference Series*, 20, ed. D. L. Lambert, 45
- Garden, R. P., Hayashi, M., Hasegawa, T., Gatley, I., & Kaifu, N. 1991, *ApJ*, 374, 540
- Gilden, D. L. 1984, *ApJ*, 279, 335
- Habe, A., & Ohta, K. 1992, *PASJ*, 44, 203
- Harris, S., Clegg, P., & Hughes, J. 1988, *MNRAS*, 235, 441
- Hausman, M. A. 1981, *ApJ*, 245, 72
- Herbig, G. H., & Bell, K. R. 1988, *Third Catalog of Emission-Line Stars of the Orion Population*, *Lick Obs. Bull.* 1111
- Lada, C. J., Elmegreen, B. G., & Blitz, L. 1978, in *IAU Colloq. 52: Protostars and Planets*, ed. T. Gehrels, 341
- Lada, J. C. & Adams, F. C. 1992, *ApJ*, 393, 278
- Lattanzio, J. C., Monaghan, J. J., Pongracic, H., & Schwarz, M. P. 1985, *MNRAS*, 215, 125
- Lee, H. -T. , Chen, W. P., Zhang, Z. -W. & Hu, Jing-Yao 2005, *ApJ*, 624, 808
- Meyer, M. R., Calvet, N., & Hillenbrand, L. A. 1997, *AJ*, 114, 288
- Mouschovias, T. C., & Morton, S. A. 1992, *ApJ*, 390, 144
- Prusti, T., Adorf, H.-M., & Meurs, E. J. A. 1992, *A&A*, 261, 685
- Rieke, G. H., & Lebofsky, M. J. 1985, *ApJ*, 288, 618
- Schieder, R., Tolls, V., & Winnewisser, G. 1989, *Experimental Astronomy*, 1, 101
- Shu, F. H., Adams, F. C., & Lizano, S. 1987, *ARA&A*, 25, 23
- Ungerechts, H., Umbanhowar, P., & Thaddeus, P. 2000, *ApJ*, 537, 221
- Vallee, J. P. 1995a, *AJ*, 110, 2256
- Vallee, J. P. 1995b, *AJ*, 109, 1724
- Walsh, W., Beck, R., Thuma, G., et al. 2002, *A&A*, 388, 7
- Wouterloot, J. G. A., & Brand, J. 1989, *A&AS*, 80, 149
- Xin, B., & Wang, J.-J. 2008, *ChJAA (Chin. J. Astron. Astrophys.)*, 8, 433
- Yang, J., Jiang, Z., Wang, M., Ju, B., & Wang, H. 2002, *ApJS*, 141, 157
- Zhou, S., Evans, N. J., II, Koempe, C., & Walmsley, C. M. 1993, *ApJ*, 404, 232